Mon. Not. R. Astron. Soc. **000**, 000–000 (0000) Printed 25 June 2014 (MN LATEX style file v2.2)

Dynamical models for the Sculptor dwarf spheroidal in a ΛCDM universe

Louis E. Strigari[1], Carlos S. Frenk[2] and Simon D. M. White[3]

[1] *Department of Physics, Indiana University, Bloomington, IN, 47405-7105 USA*
[3] *Institute for Computational Cosmology, Dep. of Physics, Univ. of Durham, South Road, Durham DH1 3LE, UK*
[3] *Max-Planck-Institut für Astrophysik, Karl-Schwarzschild-Straße 1, 85740 Garching bei München, Germany*

25 June 2014

ABSTRACT

The Sculptor dwarf spheroidal galaxy contains two distinct stellar populations: one metal-rich and the other metal-poor. Several authors have argued that in order for these two populations to reside in the same gravitational potential, the dark matter halo must have a core similar to that observed in the stellar count profile. This would rule out the cuspy Navarro-Frenk-White (NFW) density profiles predicted for halos and subhalos by dark matter only simulations of the Λ Cold Dark Matter (ΛCDM) cosmological model. We present a new theoretical framework to analyse stellar count and velocity observations in a self-consistent manner based on separable models, $f(E, J) = g(J)h(E)$, for the distribution function of an equilibrium spherical system. We use this machinery to analyse available photometric and kinematic data for the two stellar populations in Sculptor. We find, contrary to some previous claims, that the data are consistent with populations in equilibrium within an NFW dark matter potential with structural parameters in the range expected in ΛCDM. Our solution gives a maximum circular velocity for Sculptor between 20 and 35 km/s. We discuss why some previous authors came to a different conclusion.

1 INTRODUCTION

ΛCDM has emerged as the standard model of cosmic structure largely because of its successful predictions for the temperature anisotropies of the cosmic microwave background radiation, the power spectrum of the large-scale distribution of galaxies and the broad features of the galaxy formation process (see Frenk & White 2012, for a review). However, the adequacy of the model remains controversial on the small scales where the distribution of dark matter is strongly non-linear (e.g. Walker & Penarrubia 2011; Newman et al. 2013). Disagreements on these scale are particularly interesting because they could provide clues to the nature of the dark matter (e.g. Lovell et al. 2012; Peter et al. 2013; Shao et al. 2013; Zavala et al. 2013).

A robust prediction of ΛCDM is that, in the absence of baryonic effects, the spherically averaged radial density profiles of dark matter halos of all masses should approximately follow a universal form, the NFW profile (Navarro et al. 1996, 1997), which diverges as r^{-1} towards the centre. In galactic halos, baryonic effects associated with the formation of the galaxy could, in principle, flatten this central cusp through explosive events produced by supernovae, as proposed by Navarro et al. (1996) and seen more recently in a number of galaxy formation simulations (see Pontzen & Governato 2014, for a review). Energetic arguments suggest that such processes - if they do indeed occur in nature - should cease to be effective in dwarf galaxies of stellar mass between 10^6 and 10^7 $M_\odot$ which would then retain their NFW dark matter cusps (Peñarrubia et al. 2012). Although difficult to study because of their intrinsic faintness, dwarf galaxies are thus promising sites for testing ΛCDM in the strongly nonlinear regime and learning about the identity of the dark matter and the effects of baryonic processes.

The most direct way to study the central density structure of a galaxy is by fitting an equilibrium stellar dynamical model to a large sample of stars that have high resolution spectroscopy and good photometry. In recent years, data of the required quality have been obtained for a number of nearby dwarf spheroidal galaxies (dSphs) around the Milky Way (Simon & Geha 2007; Walker et al. 2009) and M31 (Tollerud et al. 2012). Simple dynamical analyses based on spherical symmetry and the Jeans equation suffer from degeneracies which preclude an unambiguous determination of the dark matter potential (Walker 2013; Strigari 2013). Thus, data for several dSphs are equally consistent with flat central profiles (cores) (Gilmore et al. 2007) or with NFW cusps (Strigari et al. 2010; Jardel & Gebhardt 2013). In some cases, degeneracies can be broken by considering higher moments of the line-of-sight velocity distribution (Richardson & Fairbairn 2014).

Sculptor, a dSph of stellar mass $\sim 10^7 M_\odot$ located ~ 80 kpc from the Galactic Centre (Lianou & Cole 2013), is a particularly interesting case. Modelling using a variety of

techniques but treating the available stellar data as sampled from a single stellar population and assuming spherical symmetry has shown that the kinematic data are consistent with an NFW halo potential, but also allow a core (Strigari et al. 2010; Breddels et al. 2013; Richardson & Fairbairn 2014). These studies suggest a dark matter halo mass of $\simeq 10^9$ $M_\odot$ for Sculptor (Łokas 2009; Strigari et al. 2010; Breddels et al. 2013).

The data for Sculptor are of sufficient quality that two distinct stellar populations of differing metallicity can be identified: a centrally concentrated metal-rich (*MR*) population and a more extended metal-poor (*MP*) population (Battaglia et al. 2008, B08). The presence of two populations makes it possible to carry out more refined dynamical analyses. Thus, applying the Jeans equation to each population separately, B08 showed that their data could be fit by a model in which the orbital distribution of each population is isotropic near the centre and becomes radially biased in the outer regions. They found a best fit for a model potential with a core but also found the data to be consistent with an NFW potential. Using Michie-King models for the stellar distribution function, Amorisco & Evans (2012) also found that while an NFW model provides an acceptable χ^2 fit to the data, models with a core seem to be preferred. On the other hand, applying the projected virial theorem, Agnello & Evans (2012) concluded that it is not possible to fit both the *MR* and the *MP* populations with a single NFW model.

An independent dynamical analysis of Sculptor using a larger sample of stars was carried out by Walker & Penarrubia (2011, WP11). Rather than simply separating the observed stars into two populations according to their estimated metallicity, they devised a statistical method which fits the full dataset simultaneously with two constant velocity dispersion, Plummer-profile populations of differing metallicity, together with a contaminating Galactic component. They then inserted the half-light radius and velocity dispersion estimated for each population into the mass estimator proposed by Walker et al. (2009). This allowed them to infer the mass contained within each half-light radius and thus the slope of the density profile between the two half-light radii. They concluded that the slope is flatter than predicted for an NFW profile at the 99% c.l.

In this study we carry out a new analysis of Sculptor in an attempt to clarify the conflicting claims in the literature. The specific statistical question we ask is whether the kinematic and photometric data for this galaxy exclude potentials of the type predicted by ΛCDM. We re-examine both the B08 and WP11 datasets from a different theoretical perspective and discuss how they compare. There are both similarities and differences between our analysis and those that have been undertaken previously. Like B08 and Amorisco & Evans (2012), but unlike Agnello & Evans (2012) and WP11, we exploit the full information contained within the line-of-sight velocity dispersion and photometry profiles. Like Amorisco & Evans (2012), but unlike B08, we build models based on distribution functions. Our analysis differs from that of Amorisco & Evans (2012) primarily in that we use a more flexible form for the distribution function which allows a wider range of energy distributions and velocity anisotropies for the stars.

We conclude, in agreement with B08 and Amorisco & Evans (2012), that NFW potentials are *not* excluded by the B08 data. In addition, we show that the half-light radii and velocity dispersions derived by WP11 from their data and used by them to exclude NFW potentials, can, in fact, be reproduced by equilibrium populations within such a potential. For our more general models the constraints used by Agnello & Evans (2012) are also no longer sufficient to exclude NFW potentials. Indeed, the implied peak circular velocity of the Sculptor dark matter halo and its concentration are consistent with the values predicted from ΛCDM simulations. While an NFW potential gives an acceptable fit to the Sculptor data, our analysis cannot exclude potentials with a core, which, based on earlier work, we would expect to give an equally good or even better fit.

This paper is organized as follows. In Section 2 we introduce our model for the stellar distribution function. In Section 3 we briefly discuss our methodology for fitting the theoretical model to the data. In Section 4 we present our results and, in Section 5, we compare them to previous studies, highlighting discrepancies where they exist.

2 MODELS

In this section we introduce the dynamical models we use to interpret the observed stellar populations in Sculptor. We assume each population to be spherically symmetric and to be in dynamical equilibrium within a static and spherically symmetric potential well. These are strong assumptions which should be treated as approximations. The observed stellar distribution is clearly non-circular on the sky, and Sculptor orbits within the potential of the Milky Way, so the effective potential seen by its stars is time varying. Some aspects of the effects of flattened potentials on the dynamical analysis of dSph data are considered by Laporte et al. (2013).

2.1 Dark matter

For the total mass density profile of the system we adopt an NFW model,

$$\rho(r) = \frac{\rho_s}{x(1+x)^2}, \tag{1}$$

with corresponding gravitational potential

$$\Phi(r) = \Phi_s \left[1 - \frac{\ln(1+x)}{x}\right], \tag{2}$$

where we define $\Phi_s = 4\pi G \rho_s r_s^2$ and $x = r/r_s$. This simple model is determined by just two scale parameters, the characteristic radius, r_s, and the characteristic density, ρ_s. Note that we define the potential to be zero at the centre of the system and to be Φ_s at infinity. NFW models are often parametrized in terms of the maximum circular velocity, V_{max}, and the radius, r_{max}, at which this is attained. These are related to r_s and Φ_s through:

$$r_{max} = 2.16\ r_s; \qquad V_{max} = 0.465\ \sqrt{\Phi_s}. \tag{3}$$

2.2 Stellar distribution function

We define the specific energy and specific angular momentum of a star as $E = v^2/2 + \Phi(r)$ and $J = vr\sin\theta$, respectively, where v is the modulus of the velocity vector and θ is the angle between this vector and the star's position vector relative to system centre. Given a static and spherically symmetric gravitational potential well, any positive definite function $f(E, J)$ corresponds to the phase-space distribution function of some stable, dynamically mixed and spherically symmetric equilibrium for a stellar population. In this paper we will consider only models in which the dependence on E and J is separable,

$$f(E, J) = g(J)h(E), \tag{4}$$

with both $g(J)$ and $h(E)$ positive definite and given by simple parametric forms. It would be easy to build more general, non-separable models as a superposition of several individually separable components, but we will not pursue this further here.

The stellar density profile and the radial and tangential stellar velocity dispersion profiles of such models are given by

$$\rho_\star(r) = 2\pi \int_0^\pi d\theta \sin\theta \int_0^{v_{esc}} dv v^2 g(J)h(E) \tag{5}$$

$$\rho_\star\sigma_r^2(r) = 2\pi \int_0^\pi d\theta \cos^2\theta \sin\theta \int_0^{v_{esc}} dv v^4 g(J)h(E) \tag{6}$$

$$\rho_\star\sigma_t^2(r) = \pi \int_0^\pi d\theta \sin^2\theta \sin\theta \int_0^{v_{esc}} dv v^4 g(J)h(E) \tag{7}$$

where $v_{esc} = \sqrt{2[\Phi_{lim} - \Phi(r)]}$. Note that with the definition we are using here the total velocity dispersion at radius r is

$$\sigma_{\rm tot}^2(r) = \sigma_r^2(r) + 2\sigma_t^2(r). \tag{8}$$

Eqns 5, 6, and 7 can be combined to give the projected stellar density profile and stellar line-of-sight velocity dispersion profile at a fixed projected distance R:

$$I_\star(R) = 2\int_0^\infty \rho_\star(r) dz, \tag{9}$$

$$I_\star(R)\sigma_{los}^2(R) = 2\int_0^\infty \rho_\star(r) \frac{z^2\sigma_r^2 + R^2\sigma_t^2}{z^2 + R^2} dz, \tag{10}$$

where $r^2 = z^2 + R^2$.

A particularly interesting and simple case occurs when the angular momentum dependence is taken to be a power law,

$$g(J) = J^b, \tag{11}$$

where $b > -2$ is a constant. For this assumption, the integrals over v and θ separate in Eqns 5, 6 and 7, and the ratio of the two velocity dispersions is independent both of r and of $h(E)$. The lower limit on b is required for the θ integrals to converge for small θ. For this choice of $g(J)$ the orbital anisotropy of the stellar population model, usually parametrized as

$$\beta(r) = 1 - \sigma_t^2(r)/\sigma_r^2(r), \tag{12}$$

is independent of radius and depends on b alone, $\beta = -b/2$. For an isotropic velocity distribution, $\beta = b = 0$. For near-radial orbits β is close to unity and b approaches its lower limit of -2, while for near-circular orbits b is very large and positive while β is very large and negative.

In this paper we will investigate models where the orbital anisotropy varies with radius and we therefore need a more general form for $g(J)$. We consider the function,

$$g(J) = \left[\left(\frac{J}{J_\beta}\right)^{\frac{b_0}{\alpha}} + \left(\frac{J}{J_\beta}\right)^{\frac{b_1}{\alpha}}\right]^\alpha, \tag{13}$$

which interpolates between a power law of index b_0 at $J \ll J_\beta$ and a power law of index b_1 at $J \gg J_\beta$. The parameter α controls the rapidity of the transition between the two regimes at the characteristic scale, J_β, which corresponds to a radius of order $r_\beta = J_\beta/\Phi_s^{1/2}$. In addition, α is required to be positive for $b_1 > b_0$ and to be negative in the opposite case.

For simplicity when comparing with the Sculptor data, we in most cases prefer to use a function with fewer free parameters and to assume that the velocity distribution is isotropic near the centre, as seems plausible on general theoretical grounds. We therefore set $|\alpha| = 1$ and $b_0 = 0$, resulting in the simpler expression

$$g(J) = \begin{cases} \left[1 + (J/J_\beta)^{-b}\right]^{-1}, & \text{for } b \le 0 \\ 1 + (J/J_\beta)^b, & \text{for } b > 0. \end{cases} \tag{14}$$

The upper and lower cases here correspond to radially and tangentially biased orbits at large angular momentum, respectively. Both produce isotropy at small angular momenta and so also at small radii. This simplified model retains only two parameters, J_β which sets the extent of the inner isotropic region and b which determines the velocity anisotropy at larger angular momenta.

For the energy distribution, $h(E)$, we have found the following form to be sufficiently general for our purposes:

$$h(E) = \begin{cases} NE^a(E^q + E_c^q)^{d/q}(\Phi_{lim} - E)^e & \text{for } E < \Phi_{lim} \\ 0 & \text{for} E \ge \Phi_{lim}, \end{cases} \tag{15}$$

where the restriction $\Phi_{lim} \le \Phi_s$ is required because orbits with $E \ge \Phi_s$ are unbound. The normalisation, N, in this expression sets the amplitude of the stellar density profile, while the exponent a determines the behaviour at small energies, hence as $r \to 0$. Comparison with the simple scale-free distribution functions explored by White (1981) shows that at sufficiently small radii (where $\Phi \ll \Phi_s$, $E \ll E_c$ and $J \ll J_\beta$)) Eqns 2, 13 and 15 imply a power-law stellar density profile, $\rho_\star \propto r^{-\gamma}$, where

$$\gamma = \begin{cases} -a - 3(b_0 + 1)/2, & \text{for } 2a + b_0 < -3, \\ -b_0, & \text{for } 2a + b_0 > -3. \end{cases} \tag{16}$$

In the first of these two cases, the density in the innermost regions is dominated by stars on orbits which are confined to those regions, while in the second it is dominated by stars on orbits which extend well beyond them. Our model for $h(E)$ thus produces a central cusp in the stellar density profile when Eqn. 16 gives $\gamma > 0$.

At somewhat larger energies, $E > E_c$ (hence at radii larger than r_c, where $\Phi(r_c) = E_c$) the density profile steepens to a new slope, γ', which is given by Eqn 16 with a replaced by $a + d$ where we assume $d < 0$. The rapidity of the transition around r_c is controlled by the parameter $q > 0$. The final factor in Eqn 15 allows for truncation of the stellar density at a radius, r_{lim}, defined by $\Phi(r_{lim}) = \Phi_{lim}$,

which is directly analogous to the "tidal radius" in the classic King models for globular clusters (King 1966). The shape of this cut-off in the profile can be adjusted using the final parameter, e. A special case arises when $\Phi_{lim} = \Phi_s$. Then $r_{lim} \to \infty$ and the density profile at large radii becomes a power law of slope $\gamma'' = e+3/2-b_1/2$ (or $\gamma'' = e+3/2-b/2$ for the simpler case of Eqn 14).

As a final remark, we note that when $\Phi_{lim} < \Phi_s$, the constraint $E < \Phi_{lim}$ forces stellar velocities and hence stellar angular momenta to be small as $r \to r_{lim}$. The anisotropy in this region is thus determined by the form of $g(J)$ for small rather than large J, with the result that $\beta = -b_0/2$ rather than $-b_1/2$ (i.e. the distribution becomes isotropic again as $r \to r_{lim}$ if the simpler parametrisation of Eqn 14 is used). This complication does not arise when $\Phi_{lim} = \Phi_s$, in which case β is indeed equal to $-b_1/2$ at large radii ($-b/2$ for the simpler model of Eqn 14).

3 DATA ANALYSIS

In this section we briefly detail the Bayesian analysis methods that we will apply to the datasets described in the following sections.

For a single stellar population, the model of Eqns 4, 14 and 15 is a function of nine parameters, $\{N, a, d, q, E_c, \Phi_{lim}, e, b, J_\beta\}$. Including the two parameters that describe the NFW potential, Eqn 2, a fit to an individual stellar population has 11 free parameters, whereas a *joint* fit to both populations (each of which has independent distribution function parameters), has a total of 20 free parameters.

We use our theoretical model to fit to the binned velocity dispersion data. We define the quantities,

$$\chi^2_{I,p} = \sum_{\imath=1}^{n_{p,I}} \frac{[I_\star(R_\imath) - I_p(R_\imath)]^2}{\delta^2_{p,\imath}}, \quad (17)$$

$$\chi^2_{\sigma,p} = \sum_{\imath=1}^{n_{p,\sigma}} \frac{[\sigma_{los}(R_\imath) - \sigma_p(R_\imath)]^2}{\epsilon^2_{p,\imath}}, \quad (18)$$

where the subscript, p, denotes a specific population, either MR or MP. Additionally $n_{p,I}$ is the number of data points in the photometric profile of a population, and $n_{p,\sigma}$ the number of data points in the velocity dispersion profile of a population, both of which are measured at projected distance, $R_\imath$. The associated measurement uncertainties are $\delta_{p,\imath}$ and $\epsilon_{p,\imath}$. Using these quantities we define a full likelihood function of the form,

$$-2\ln\mathcal{L} = \chi^2_{total} + \text{const}, \quad (19)$$

where

$$\chi^2_{total} = \chi^2_{I,MR} + \chi^2_{\sigma,MR} + \chi^2_{I,MP} + \chi^2_{\sigma,MP}. \quad (20)$$

The constant in Eqn 19 depends on the photometric and velocity dispersion measurement uncertainties but does not depend on the distribution function model.

We employ an MCMC algorithm which is an adapted version of the CosmoMC code (Lewis & Bridle 2002). From this algorithm we can extract two important quantities: (i) the maximum value of the likelihood, $\mathcal{L}_{max}$, which corresponds to a minimum value of χ^2_{total} and to the "best fit" set of parameters from a given chain, and (ii) the posterior probability distribution for each model parameter. For scans of a large and complex theoretical parameter space, MCMC algorithms are not necessarily effective at finding the true value of $\mathcal{L}_{max}$, so it is important to determine if the estimated value of $\mathcal{L}_{max}$ corresponds to a set of theoretical parameters that provide a statistically good fit to the data. We thus run several chains from different starting points in the theoretical parameter space to ensure that the chains find similar values of $\mathcal{L}_{max}$ and are thus not burning in at local maxima in the likelihood.

The fact that we are marginalizing over up to twenty parameters also means that we must test that the posterior probability distributions for the model parameters have appropriately converged. We test for convergence of the posterior probability distributions in a standard manner by estimating the variance of a parameter as a weighted sum of the within-chain and between-chain variance (Gelman & Rubin 1992).

4 RESULTS

B08 obtained spectroscopy for 470 stars in Sculptor from which they measured line-of-sight velocities and metallicites derived from the Calcium triplet lines. They identified two distinct populations with different metallicity, spatial distribution and kinematics: a metal rich (MR) population, defined to have $[Fe/H] > -1.5$, and a metal poor (MP) population, defined to have $[Fe/H] < -1.7$. This clean separation and the large radial coverage of the two populations make this an attractive sample to analyze using our model distribution function described in Section 2. We fit our distribution function model to the photometric and velocity dispersion profiles reported by B08 for each population by performing a likelihood analysis using the MCMC technique, as described in Section 3.

Since the stellar distribution of Sculptor is elongated on the sky, B08 give the surface brightness profile of each population as a function of an "elliptical radius" which corresponds to the projected semi-major axis determined from the photometry (Tolstoy et al. 2004). To account for this within the context of our assumption of spherical symmetry, we take as the radial coordinate the geometric mean of the major and minor axes, which we expect to correspond best to the count profile for circular annuli. The ellipticity of Sculptor is $\epsilon = 0.3$ (Irwin & Hatzidimitriou 1995).

We fit the full stellar density and velocity dispersion profiles of the two metallicity populations to the 20-parameter model defined in Section 2, which assumes an NFW potential, and in which the velocity anisotropy can vary with radius but is assumed isotropic at the centre. From the MCMC chains we obtain both the maximum likelihood value and the posterior probability distribution for each model parameter. The surface density and velocity dispersion profiles for a model that has near-maximal likelihood are shown in Figure 1. The count profiles of both stellar populations exhibit well-defined cores. The MP population in this particular model is isotropic everywhere, while the MR population is isotropic in the centre, has a sharp transition at a scale radius of ~ 0.2 kpc to $\beta \simeq 0.94$ over the range $0.2 - 1$ kpc, and then transitions smoothly back to $\beta = 0$ at

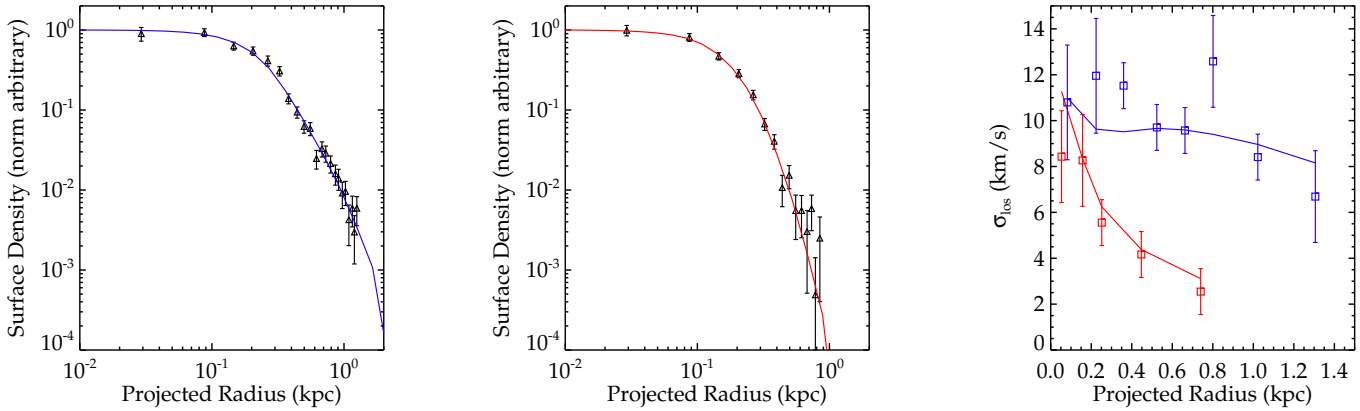

Figure 1. Best-fit model of Eqns. 14 and 15 to the Battaglia et al. (2008) data for the metal-poor and metal-rich populations in Sculptor, assuming an NFW potential. The left and middle panels show the surface brightness profiles of the *MP* and *MR* populations respectively; the right panel shows the velocity dispersion profile of the *MP* population (blue line at the top) and the *MR* population (red line at the bottom).

larger radii in order to satisfy the boundary conditions at r_{lim}. The parameters of this model are listed in Table 1.

Figure 1 shows that the data for the two metallicty populations in Sculptor are very well fit by our model, and this impression is confirmed by the values of χ^2 for the fits: 21.6 for the *MP* photometry (left; 23 data points), 8.8 for the *MR* photometry (middle; 15 data points), 8.3 for the *MP* kinematics (upper right; 8 data points), and 1.5 for the MR kinematics (lower right; 5 data points). Our analysis therefore demonstrates that the data are consistent with both metallicity populations residing in a single NFW potential.

Consistency with a potential of the NFW form alone, however, does not guarantee that the data are also consistent with the predictions of the ΛCDM model. For this to be the case, the parameters of the NFW density profile must lie within the theoretically predicted range. The comparison is most easily carried out in (V_{max}, r_{max}) space, where the maximum circular velocity of the dark matter halo, V_{max}, and the radius, r_{max}, at which it is attained are defined in Eqn. 3 and are readily measured for subhalos in high resolution ΛCDM N-body simulations of galactic halos.

The region in the (V_{max}, r_{max}) plane in which 90% of the subhalos in the "Aquarius" ΛCDM simulations of Springel et al. (2008) lie is shown by the thin lines in Figure 2. The thick lines show the 68% and 90% contours of two-dimensional joint posterior probability distributions of V_{max} and r_{max} derived from our fits to the B08 data. That these contours overlap with the theoretically predicted region demonstrates that the kinematics of the populations in Sculptor are fully consistent with expectations in a ΛCDM universe. The range of V_{max} allowed by our fits $\sim (20-35)$ km/s, is significantly wider range than the range estimated in previous analyses (Boylan-Kolchin et al. 2011).

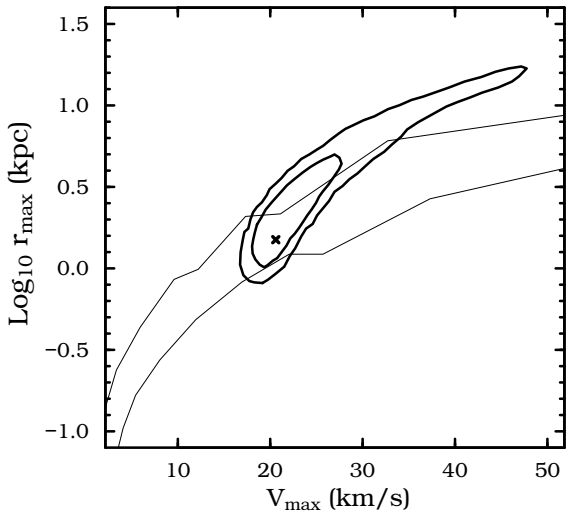

Figure 2. The 68% and 90% c.l. regions in the $V_{max}-r_{max}$ plane for fits to the model of Eqns. 14 and 15 to the two metallicity populations in Sculptor (thick lines). A cross indicates the model of Table 1. Thin lines delineate the region which contains 90% of the subhalos from the Aquarius ΛCDM simulations of galactic halos (Springel et al. 2008).

5 COMPARISON TO PREVIOUS RESULTS

Several previous studies have constrained the potential in Sculptor by splitting its stars into high and low metallicity populations and requiring each separately to be in equilibrium. In this section we compare our results with these earlier analyses.

5.1 Battaglia et al. (2008)

In the first dynamical analysis to separate the two populations in Sculptor, B08 applied the Jeans equation to each population individually, fitting the star count profiles to standard forms (Plummer for the metal-rich, Sersic for the metal-poor) and then predicting the velocity dispersion profiles for various assumed potentials and anisotropy profiles. They found that their data were consistent with both NFW

Population	a	d	e	E_c	Φ_{lim}	r_{lim}	b	q	J_β	V_{max}	r_{max}
MR	2.0	-5.3	2.5	0.16	0.45	1.5	-9.0	6.9	8.6×10^{-2}	21	1.5
MP	2.4	-7.9	1.1	0.17	0.60	3.0	0	8.2	–		

Table 1. An example distribution function model that provides a good fit to the Sculptor two-population data. E_c and Φ_{lim} are in units of Φ_s and, for the MR population, J_β is in units of $r_s\sqrt{\Phi_s}$; V_{max} is in km/s and r_{max} in kpc.

and core potentials, but required radially biased orbits for both populations.

Our results largely corroborate the conclusions reached by B08. Our use of a flexible stellar distribution function removes the need to assume standard forms for the count and anisotropy profiles and ensures that the resulting model is physically realizable. As a result, our best-fit model has a smaller χ^2 than the model of B08. Like B08, we find that radially-biased orbits are required at large radius for the metal-rich (although not for the metal-poor) population.

5.2 Amorisco & Evans (2012)

Of the previous studies, that of Amorisco & Evans (2012) is most similar to our own. They also assumed separable distribution functions for the two populations and fit predicted counts and velocity dispersion profiles to the data of B08. They considered both NFW potentials and pseudo-isothermal potentials with a core. Although the form they assumed for their distribution functions is considerably less flexible than our own, the resulting best fit for an NFW potential is similar to ours, shown in Fig. 1, and has a χ^2 value which is clearly insufficient to exclude the model. The best fit for the core case also looks similar (compare their figures 9 and 10). Nevertheless, its χ^2 value is sufficiently smaller that a likelihood ratio test clearly prefers it over an NFW potential.

As Amorisco & Evans (2012) note, the preference for a core potential over a cuspy one is driven in their analysis by its lower prediction for the innermost points of the count profiles and, to a lesser extent, by a somewhat larger predicted difference in velocity dispersion between the two populations. With our more flexible distribution function model, the count discrepancy at small radius disappears for the NFW potential and the difference in velocity dispersions between the *MP* and *MR* populations is slightly enhanced (see Fig. 1), leading to a fit of very similar quality to that found by Amorisco & Evans (2012) for their core potential. A final difference with Amorisco & Evans (2012) is that their NFW fit required a halo concentration which is lower than expected in ΛCDM. With our distribution function model, this problem has disappeared.

5.3 Agnello & Evans (2012)

Agnello & Evans (2012) applied the projected virial theorem separately to the two populations identified by B08 assuming that they reside in an NFW potential and have Plummer-law surface brightness profiles. With these assumptions, the observational data for each population imply a relation between V_{max} and r_{max} for its halo. They then show that the regions of the (V_{max}, r_{max}) plane allowed at 2σ by the *MR* and *MP* data do not overlap. They therefore conclude that no single NFW potential can accommodate both populations.

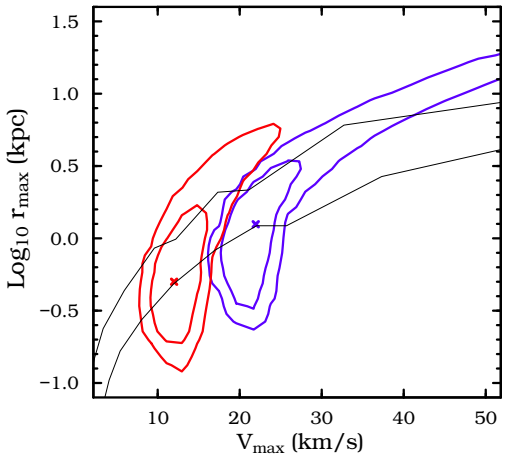

Figure 3. The 68% and 95% c.l. contours in the $V_{max} - r_{max}$ plane for *independent* fits to the two metallicity populations in Sculptor. The red contours are obtained from fitting the 11 parameter model of Eqns. 14 and 15 to the B08 *MR* data, while the blue contours are obtained from fitting the 11 parameter model to the B08 *MP* data. Crosses in each case indicate the best-fit model.

B08 noted that the metal-poor population in Sculptor is poorly fit by a Plummer model. By applying our procedures to the *MR* and *MP* data separately, we can perform an analysis analogous to that of Agnello & Evans (2012). In Figure 3 we show the two-dimensional joint posterior probability distributions of (V_{max}, r_{max}). We indeed reproduce an offset similar to that seen by Agnello & Evans (2012). However, the greater freedom afforded by our relaxation of the Plummer-law assumption, allowing instead any profile consistent with the observed counts, widens the confidence regions so that that are no longer exclusive. The two distributions are marginally consistent with each other for $V_{max} \sim (15-25)$ km/s and $r_{max} \sim 1$ kpc which, not suprisingly, is the region also picked out by our single potential model. As before, these parameters are consistent with the ΛCDM predictions of Springel et al. (2008).

5.4 Walker & Penarrubia (2011)

WP11 analyzed a sample of 1497 stars with spectroscopy from which they derive line-of-sight velocities and an Mg index which they take as a proxy for metallicity. They use MCMC techniques to map the parameter distributions for a 3-component model of these data. The metal-rich and metal-poor populations are each represented by a circularly symmetric Plummer profile, with Gaussian velocity and metal-

licity distributions independent of radius, while the contaminating Galactic foreground is taken to be spatially uniform with broader distributions of velocity and metallicity. They then insert the half-light radius and velocity dispersion obtained for each population into the mass estimator proposed by Walker et al. (2009):

$$M_h = M(R_h) = 2.5\langle\sigma_{los}^2\rangle R_h/G, \qquad (21)$$

which gives the mass, M_h, inside a sphere with radius equal to the projected half-light radius, R_h, in terms of the measured velocity dispersion, σ_{los}^2, and R_h[1]. The derived increase in estimated mass between the two values of R_h appears too large to be consistent with an NFW profile and is close to that expected for a constant density core. WP11 conclude that NFW is excluded at the 99% c.l.

This conclusion is incompatible with our own, based on the B08 data. In Fig. 4 we show the results of WP11 in the (R_h, M_h) plane, together with lines corresponding to $M \propto r^\gamma$, with $\gamma = 2$ and $\gamma = 3$. Clearly, these results agree much better with the dotted line representing a core than with the dashed line representing an NFW cusp. Our distribution function based MCMC analysis allows us to reconstruct R_h and M_h for all models consistent with the B08 data and residing in an NFW potential. Solid red and blue contours in Fig. 4 give the 68% and 90% confidence regions for the metal-rich and metal-poor populations respectively. As expected, the centre points of these contours define a slightly shallower slope than the dashed line since $\gamma = 2$ only in the innermost regions of an NFW profile. The half-light radii found for the *MR* and *MP* populations in the two analyses agree well but there is a clear offset in the derived M_h values, although the contours do overlap. Hence, fitting our models to the B08 data has resulted in lower velocity dispersions for the *MP* and higher velocity dispersions for the *MR* than estimated by WP11 from their own data.

This discrepancy could reflect differences in analysis or between the B08 and WP11 datasets. To investigate this further we compare in Fig. 5 the (R_h, σ_{los}) values inferred for the two underlying populations by WP11 with those inferred directly for the observed populations from the B08 data. We obtain the latter by numerically integrating the count and velocity dispersion data shown in Fig. 1. Although the values of R_h obtained from the two datasets agree well, the value of σ_{los} in WP11 is noticeably lower for the *MR* population, and is noticeably higher for the *MP* population than in B08. The shifts, however, are at the 1σ level. Some shift may be expected because the two observed populations of B08 may mix the two underlying populations of WP11, but it cannot be large given the excellent agreement in the characteristic radii inferred from the two studies.

Fig. 5 also shows contours from our MCMC analysis constrained to fit both B08 populations in a single NFW potential. The prior imposed by this constraint biases the σ_{los} estimate high by about 0.5σ for the *MR* population and low by about 1σ for the *MP* population, thus enhancing the offset from the WP11 estimates. Hence, the differing conclusions in WP11 and in this paper are due, in part, to differences in the data analyzed and, in part, to a difference in the statistical question addressed: WP11 ask which profile slope best fits their estimated (R_h, σ_{los}) values, whereas we ask whether the B08 observations are able to exclude an NFW potential.

An additional uncertainty in the approach of WP11 comes from the assumption that the coefficient in Eqn. 21 is

[1] This estimator is constructed to be only weakly sensitive to the details of the density and velocity anisotropy profiles (see also Wolf et al. 2010)

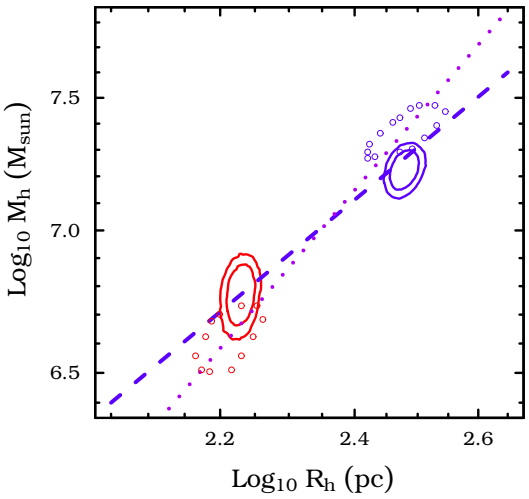

Figure 4. Constraints from WP11 and from the models of this paper in the (R_h, M_h) plane. The two straight lines and the contours traced by open circles are taken directly from Figure 10 of WP11 and indicate $M \propto r^\alpha$ with $\alpha = 2, 3$ and the 50% c.l. regions given by their MCMC analysis for the parameters of the two underlying populations. For comparison, the solid contours show 68% and 90% c.l. regions from our own MCMC chains constrained by the B08 data and assuming both populations to be in equilibrium within a single NFW potential.

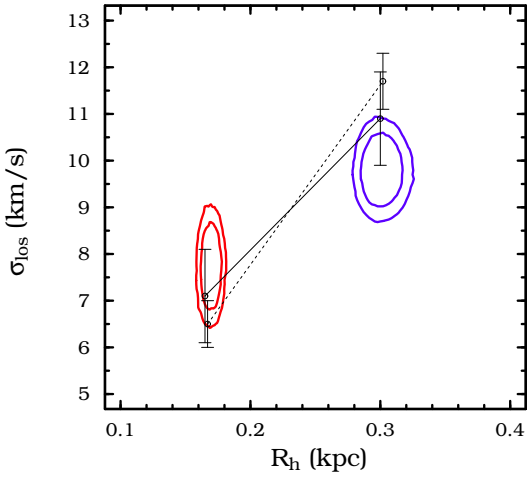

Figure 5. Overall light-weighted line-of-sight velocity dispersion *vs* projected half-light radius. The dots linked by a solid line correspond to the B08 *MR* and *MP* populations and the dots linked by a dotted line to the two WP11 populations. The contours are 68% and 90% c.l. from MCMC chains for our stellar distribution function models constrained by the B08 data and required to be in equilibirum in a single NFW potential.

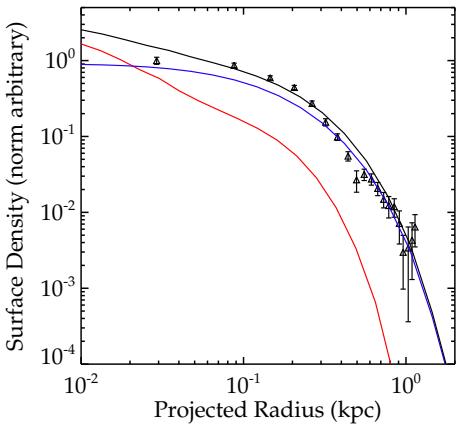

Figure 6. A distribution function based model required to fit the R_h, M_h data of WP11 precisely, and the total count profile data of B08 (black points) approximately, with both populations in equilibrium in an NFW potential. The red, blue and black curves show projected count profiles for the *MR* and *MP* populations and their sum, respectively. The fact that such a model can be found demonstrates that the WP11 data alone are not sufficient to exclude an NFW potential.

independent of the detailed structure of each component. We have checked the relation between M_h, R_h and σ_{los} for the *MR* and *MP* populations in the best fit model of Fig. 1, finding values of 2.80 and 2.66 in the two cases, rather than the 2.5 of Eqn. 21. WP11 argued that they expect this equation to overstimate M_h for both populations and more strongly for the inner one. In fact, we find the opposite for our model. For both populations Eqn. 21 underestimates M_h and this underestimate is by a larger factor for the inner population. This bias adds to the apparent discrepancy between the WP11 analysis and our own.

To investigate this issue further, we ask whether it is possible to find equilibrium populations in a single NFW potential which reproduce the actual (R_h, σ_{los}) values inferred by WP11 for their two populations. We re-run our MCMC machinery using these values as constraints with very small error bars while using the total count profile from B08 as an additional, weaker constraint. The best fit found by this procedure is shown in Fig. 6. The two populations here reproduce the WP11 (R_h, σ_{los}) values essentially perfectly and are an approximate fit to the B08 counts. Although the shapes of the *MR* and *MP* profiles are not consistent in detail with the B08 data, this example proves that the data used by WP11 in their own analysis *can* be fit by equilibrium populations in an NFW potential. Hence, their analysis alone is not enough to exclude such a potential.

6 CONCLUSIONS

In this paper we have presented a new distribution function based framework to study stellar populations in equlibrium within a spherical dark matter potential well. We use it to study the two metallicity populations in the Sculptor dwarf spheroidal galaxy, in particular, to explore the controversial question of whether their properties exclude a cuspy profile of the kind expected in the ΛCDM cosmology.

The family of distribution functions we consider gives substantially more freedom than the models assumed in previous studies and, as a result, leads to a weaking of the constraints implied by the observations. Although in the absence of any prior on the shape of the inner potential, we concur with previous studies that the Sculptor data prefer a shallower profile than NFW, we find this preference to be far too weak to exclude the cosmological prediction. Indeed, in a χ^2 sense, we are able to find equilibrium models which are a good fit to the data of B08 within an NFW potential with parameters that are fully consistent with ΛCDM.

Since the inner structure of dwarf galaxies appears at present as one of the few significant challenges to the standard cosmological paradigm it is unsurprising that considerable attention is focused on measuring this structure precisely. Unfortunately, the problem is underconstrained by currently available data, given the considerable freedom inherent in the equations of stellar dynamics. The analysis in this paper, while comparatively general, still makes at least two major assumptions which are known to be incorrect: dwarf spheroidal galaxies are clearly not spherically symmetric and their orbits within the Milky Way's potential ensure that most cannot be static systems in equilibrium. Further theoretical progress will require these shortcomings to be addressed. Further observational progress may be achieved by reducing the statistical and measurement uncertainties and, in the more distant future, by increasing the phase-space coverage through measurement of internal proper motions.

7 ACKNOWLEDGEMENTS

We would like to thank Chervin Laporte for his critical comments on an earlier version of this work which prompted us to develop the distribution function methods used in this paper. LES acknowledges support from National Science Foundation grant PHY-1417457. This material is based upon work supported by the National Science Foundation under Grant No. CNS-0723054. CSF acknowledges ERC Advanced Investigator Grant COSMIWAY and SDMW ERC Advanced Investigator Grant GALFORMOD. This work was supported in part by an STFC rolling grant to the ICC.

REFERENCES

Agnello A., Evans N. W., 2012, ApJ Lett, 754, L39
Amorisco N. C., Evans N. W., 2012, MNRAS, 419, 184
Battaglia G., Helmi A., Tolstoy E., Irwin M., Hill V., Jablonka P., 2008, ApJ Lett, 681, L13
Boylan-Kolchin M., Bullock J. S., Kaplinghat M., 2011, Mon.Not.Roy.Astron.Soc., 415, L40
Breddels M. A., Helmi A., van den Bosch R. C. E., van de Ven G., Battaglia G., 2013, MNRAS, 433, 3173
Frenk C. S., White S. D. M., 2012, Annalen der Physik, 524, 507
Gelman S., Rubin D., 1992, Statistical Science, 7, 457?472
Gilmore G., Wilkinson M. I., Wyse R. F. G., Kleyna J. T., Koch A., Evans N. W., Grebel E. K., 2007, ApJ, 663, 948

Irwin M., Hatzidimitriou D., 1995, Mon.Not.Roy.Astron.Soc., 277, 1354
Jardel J. R., Gebhardt K., 2013, Astrophys.J., 775, L30
King I. R., 1966, AJ, 71, 64
Laporte C. F. P., Walker M. G., Peñarrubia J., 2013, MNRAS, 433, L54
Lewis A., Bridle S., 2002, Phys.Rev., D66, 103511
Lianou S., Cole A. A., 2013, A&A, 549, A47
Łokas E. L., 2009, MNRAS, 394, L102
Lovell M. R., Eke V., Frenk C. S., Gao L., Jenkins A., Theuns T., Wang J., White S. D. M., Boyarsky A., Ruchayskiy O., 2012, MNRAS, 420, 2318
Navarro J. F., Eke V. R., Frenk C. S., 1996, MNRAS, 283, L72
Navarro J. F., Frenk C. S., White S. D. M., 1996, ApJ, 462, 563
Navarro J. F., Frenk C. S., White S. D. M., 1997, ApJ, 490, 493
Newman A. B., Treu T., Ellis R. S., Sand D. J., 2013, ApJ, 765, 25
Peñarrubia J., Pontzen A., Walker M. G., Koposov S. E., 2012, ApJ Lett, 759, L42
Peter A. H. G., Rocha M., Bullock J. S., Kaplinghat M., 2013, MNRAS, 430, 105
Pontzen A., Governato F., 2014, Nature, 506, 171
Richardson T., Fairbairn M., 2014, MNRAS, 441, 1584
Shao S., Gao L., Theuns T., Frenk C. S., 2013, MNRAS, 430, 2346
Simon J. D., Geha M., 2007, Astrophys.J., 670, 313
Springel V., Wang J., Vogelsberger M., Ludlow A., Jenkins A., et al., 2008, Mon.Not.Roy.Astron.Soc., 391, 1685
Strigari L. E., 2013, Phys.Rept., 531, 1
Strigari L. E., Frenk C. S., White S. D., 2010, Mon.Not.Roy.Astron.Soc., 408, 2364
Tollerud E. J., Beaton R. L., Geha M. C., Bullock J. S., Guhathakurta P., et al., 2012, Astrophys.J., 752, 45
Tolstoy E., Irwin M. J., Helmi A., Battaglia G., Jablonka P., Hill V., Venn K. A., Shetrone M. D., Letarte B., Cole A. A., Primas F., Francois P., Arimoto N., Sadakane K., Kaufer A., Szeifert T., Abel T., 2004, ApJ Lett, 617, L119
Walker M., 2013, Planets, Stars and Stellar Systems. Volume 5: Galactic Structure and Stellar Populations, Oswalt, T. D. and Gilmore, G., 1039, p. 1039
Walker M. G., Mateo M., Olszewski E. W., 2009, AJ, 137, 3100
Walker M. G., Mateo M., Olszewski E. W., Penarrubia J., Evans N. W., et al., 2009, Astrophys.J., 704, 1274
Walker M. G., Penarrubia J., 2011, Astrophys.J., 742, 20
White S. D. M., 1981, MNRAS, 195, 1037
Wolf J., Martinez G. D., Bullock J. S., Kaplinghat M., Geha M., et al., 2010, Mon.Not.Roy.Astron.Soc., 406, 1220
Zavala J., Vogelsberger M., Walker M. G., 2013, MNRAS, 431, L20